Available online at www.sciencedirect.com

jmr&t Journal of Materials Research and Technology

journal homepage: www.elsevier.com/locate/jmrt

Original Article

# The effect of temperature and strain rate on the mechanical properties and microstructure of super Cr13 martensitic stainless steel

*Hamed Aghajani Derazkola* [a,b,*], *Eduardo Garcia* [a], *Alberto Murillo-Marrodán* [a], *Jens Hardell* [b]

[a] *Department of Mechanics, Design and Industrial Management, University of Deusto, 48007 Bilbao, Spain*
[b] *Department of Applied Physics and Mechanical Engineering, Luleå University of Technology, Luleå, 97187, Sweden*

ARTICLE INFO

*Article history:*
Received 4 January 2023
Accepted 3 April 2023
Available online 6 April 2023

*Keywords:*
Super Cr13
Hot tensile test
Elevated temperature
High strain rate
Microstructure analysis
Fractography

ABSTRACT

In this study, the formability of super Cr13 martensitic stainless steel (MSS) is examined by means of hot tensile tests at different temperatures (900°C–1100 °C) and t strain rates ($0.01s^{-1}$-$10s^{-1}$). The potential effect of strain rates and temperatures on the mechanical properties, microstructure and fracture surface of super Cr13 MSS were examined. The post-test analysis, which includes hardness measurements, X-ray diffraction (XRD), fracture analysis by scanning electron microscope (SEM), and Energy-dispersive X-ray spectroscopy (EDS), was carried out. Results show that ultimate tensile stress (UTS) decreases with temperature, this way, the highest UTS was obtained at 900°C-$10s^{-1}$ (187 MPa), while the lowest UTS (38 MPa) was obtained in the 1100°C-$0.01s^{-1}$ sample. By contrast the elongation of the material increases with strain rate, since the elongation of the sample at 900°C-$10s^{-1}$ was near 16% and the elongation of the sample at 1100°C-$0.01s^{-1}$ was 57%. The XRD and EDS analysis indicated that $Cr_{23}C_6$ and $Cr_2N$ are formed inside the microstructure of samples tested between 900 °C and 1000 °C, and these carbides are dissolved above 1000 °C. Temperature affects also retained austenite which increases with temperature. Fractography analysis indicated that the δ-ferrite phase has a primary role in high-temperature rapture. Fracture surface evaluation of samples revealed semi-ductile fracture behaviour below 1000 °C and low strain rates, while ductile fracture was detected on the tensile samples at temperatures higher than 1000 °C and high strain rates. Furthermore, the ductility of super Cr13 MSS was increased by increasing strain rate.



* Corresponding author.
E-mail address: h.aghajani@deusto.es (H.A. Derazkola).
https://doi.org/10.1016/j.jmrt.2023.04.012

## 1. Introduction

Super Cr13 stainless steel is a member of the martensitic stainless steel (MSS) family with low carbon content. Super Cr13 is composed mainly of Iron (Fe), Chromium (Cr), Nickel (Ni), and Molybdenum (Mo) as primary elements [1]. In different standards, the super Cr13 stainless steel is named Cr13Ni5Mo2, EN 1.4415, or S41426. During the production of this alloy, a specific amount of Cr and C is used to have stainless characteristics and ensure the formation of a martensitic structure after a complete cycle of heat treatment [2]. Due to the instability of the austenite phase in steel with more than 10% chromium, nickel is added into Super Cr13 compositions. By adding Ni to the steel structure, the formation of δ-ferrite minimizes, then depressing the Ac1 temperature and increasing Ac3 temperatures in the equilibrium phase diagram that leads to the stability of the austenite phase in steel [3]. During MSS production, the temperatures in the furnace are high enough (more than 1000 °C) to transform the steel structure into austenite [4]. After cooling in air, the microstructure of MSS will transform allotropically into the martensite phase [5]. Implementing quenching or tempering heat treatments makes it possible to attain a wide range of tensile strength, wear, and corrosion resistance for super Cr13 stainless steel [6], and for this reason, it is widely used in the petrochemical, energy, and transport industries.

Due to the specific properties of Super Cr13 steel, like high thermal and corrosion resistance, high strength, and toughness, the formability of this alloy is a challenging topic in manufacturing engineering [7]. Analyzing material behavior under various strains and stress is the foremost step to the manufacturability of a metallic material [8]. Skew mills, ring rolling, forging, deep drawing draw benches for tube and rod, and extrusion are samples of manufacturing processes widely used to produce different components from super Cr13 stainless steel [9]. Seamless tubes are one of the main components produced by super Cr13 stainless steel [10], which are usually obtained by hot metal forming processes. Controlling the microstructure and fracture phenomena of super Cr13 steel will help producing defect free seamless tubes. However, many issues can affect the formability and material behaviour during thermo-mechanical processing [11]. Hot formability refers to the workability of a material above half of its melting temperature (0.5 Tm) [12]. It is shown that MSS has good workability. The MSS yield strength and the hardness decrease above 0.5 Tm, but the ductility increases [13]. There are various methods to evaluate the formability of metallic materials. Hot compression and uniaxial tensile tests are the main standard procedures providing information about material behaviour during hot forming processes. Depending on the manufacturing processes and workpiece material properties information, the type of hot formability test is selected. The main difference between the tests mentioned is that fracture analysis of the desired metal is only possible in hot tensile tests. Accordingly, the hot tensile test suits metals exposed to large deformation with a high strain rate at high temperatures [14].

Based on hot compression test of MSS, and with the experimental results, mathematical models were presented to relate the stress-strain information to the microstructure of MSS [15]. According to the available literature, a few studies focused on the hot tensile behaviour of MSS. Li et al. [16] investigated the austenite transformation behaviour during the hot tensile test of the duplex steel. They considered temperature ranges from 950 °C to 1150 °C, with a fixed strain rate. They stated that the secondary austenite transformation occurs during the cooling process of the hot tensile test. Deng et al. [17] analysed microcrack phenomena during hot tensile tests of 2101 duplex steel. According to their results, the continuous dynamic recrystallization (CDRX) phenomenon is the leading softening mechanism in this steel during the test. The void accumulation is the primary fracture mechanism in the microstructure of 2101 duplex steel during the hot tensile test. Salas-Reyes et al. [18] studied the effect of boron content on the hot mechanical behaviour of TWIP steel. They reported that adding boron during the casting of this steel benefits the ductile behaviour in hot conditions. Shaikh et al. [16] simulated the hot tensile behaviour of ferritic/martensitic stainless (13CrMoNbV) steel with the finite element method. They modified Rice and Tracy fracture criteria and supposed that fracture type was ductile. Also, they used a modified Arrhenius constitutive model to simulate the material behaviour. They reported that the modified equations agree well with experimental results from the aforementioned material.

The review of the available literature shows that the thermo-mechanical changes of Super Cr13 martensitic stainless steel have not been considered. For this reason, the flow curves of super Cr13 steel during the hot tensile test have been obtained. The microstructural changes and fractography of the sample after the mechanical tests were evaluated and correlated with chemical changes and hardness assessed.

## 2. Experimental procedure

In this study, super Cr13 martensitic stainless steel, supplied by Tubos Reunidos [19], was used in the experimental tests. The chemical composition is presented in Table 1.

The samples in as-delivered condition (no heat treatment) were prepared for a hot tensile test. The microstructure of super Cr13 is depicted in Fig. 1a, which contains delta ferrite on the martensite matrix and all samples have the same uniform microstructure (in all parts of the sample). Hot tensile samples were prepared on a turning lathe according to the ASTM E21-09 (2020) and ASTM-E08M-E04 (2021) standards. A modified hot tensile STM-250 machine was employed for tests. A picture of the hot tensile sample is depicted in Fig. 1b. The prepared samples were placed on the hot tensile test machine with a

**Table 1 – Chemical composition of Super Cr13 martensitic stainless steel.**

| Element | C | Cr | Ni | Mn | Si | Mo | P | S | Ti | V | Fe |
|---|---|---|---|---|---|---|---|---|---|---|---|
| Wt.% | 0.03 | 11.5 to 13.5 | 4.5 to 6.5 | 0.5 | 0.5 | 1.5 to 3 | 0.02 | 0.005 | 0.01 to 0.5 | 0.5 | Bal. |

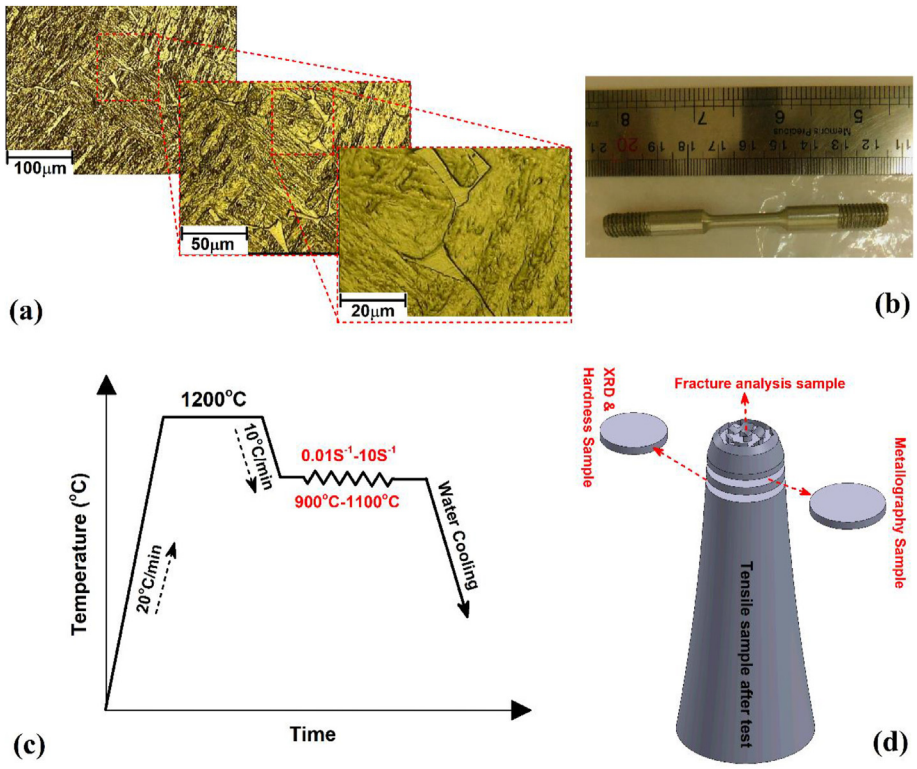


**Fig. 1 – (a) microstructure of as-delivered super Cr13, (b) prepared hot tensile sample, (c) schematic of hot tensile test temperature profile, and (d) schematic view of characterization samples.**

resistance heating system. The machine was equipped with a K-type thermocouple and was able to apply various strain rates and maximum temperature of 1100 °C on the tensile sample during the test. The sample was placed on the machine and heated up from room temperature up to 1200 °C with a 20 °C/min heating rate. The total heating time was nearly 60 min, and after that, the sample was kept at the highest temperature for 20 min. Then the sample was cooled down (by 10 °C/min) to the desired temperature for the test. This study focussed on the hot tensile at 900 °C, 1000 °C, and 1100 °C with $0.01s^{-1}$, $0.1s^{-1}$, $1s^{-1}$, and $10s^{-1}$ strain rates (Fig. 1c). To better follow the test procedure, all samples are labelled by numbers. The experiment conditions and sample are presented in Table 2.

All test conditions are repeated two times, and average results are reported. Immediately when the test finished, the sample was quenched in cold-temperature water (0°c). The cold-water quenching was selected to minimize the static dynamic recrystallization (SDRX) after tests and find more information about microstructure changes for each test. A schematic of the hot tensile test temperature profile is depicted in Fig. 1c. After the test, the tensile sample was cut into three pieces for the characterization, as depicted in Fig. 1d. The fracture area was selected for fractographic analysis with scanning electron microscopy (SEM).

**Table 2 – Test condition for each sample.**

| Sample Number | Temperature (°C) | Strain rate ($s^{-1}$) |
|---|---|---|
| 1 | 900 | 0.01 |
| 2 | 900 | 0.1 |
| 3 | 900 | 1 |
| 4 | 900 | 10 |
| 5 | 1000 | 0.01 |
| 6 | 1000 | 0.1 |
| 7 | 1000 | 1 |
| 8 | 1000 | 10 |
| 9 | 1100 | 0.01 |
| 10 | 1100 | 0.1 |
| 11 | 1100 | 1 |
| 12 | 1100 | 10 |

For chemical analysis, an X-ray diffraction (XRD) has been carried out in the range of 0–100°, 0.5 s counting time, 30 mA current, and 40 kV voltage. The XRD tests were carried out according to the EN 13925-1 standard. After the tests, the hardness of all samples was evaluated by Vickers microhardness. The hardness tests were carried out by Shimadzu micro-hardness device with 300 gf for 15 s according to the ASTM E384-17 standard. The microstructural evaluation has been done for the analysis of samples after tests. The samples were prepared according to the ASTM E3-17 and after polishing, the samples were micro-etched according to the ASTM E–407 (2015) standard using Vilella reagent (1gr picric acid+ 5 ml hydrochloric acid + 100 ml ethanol) as the etchant. An optical microscope was used to picture samples according to the ASTM E883-17 standard, and after that, ImageJ software was implemented to measure the average grain size of samples after the test. For better sample analysis tracking of temperature effect and strain rate effects, samples 1, 9, and 12 were evaluated and presented in detail. The comparison between samples 1 and 9 was for the analysis of temperature effects. A comparison

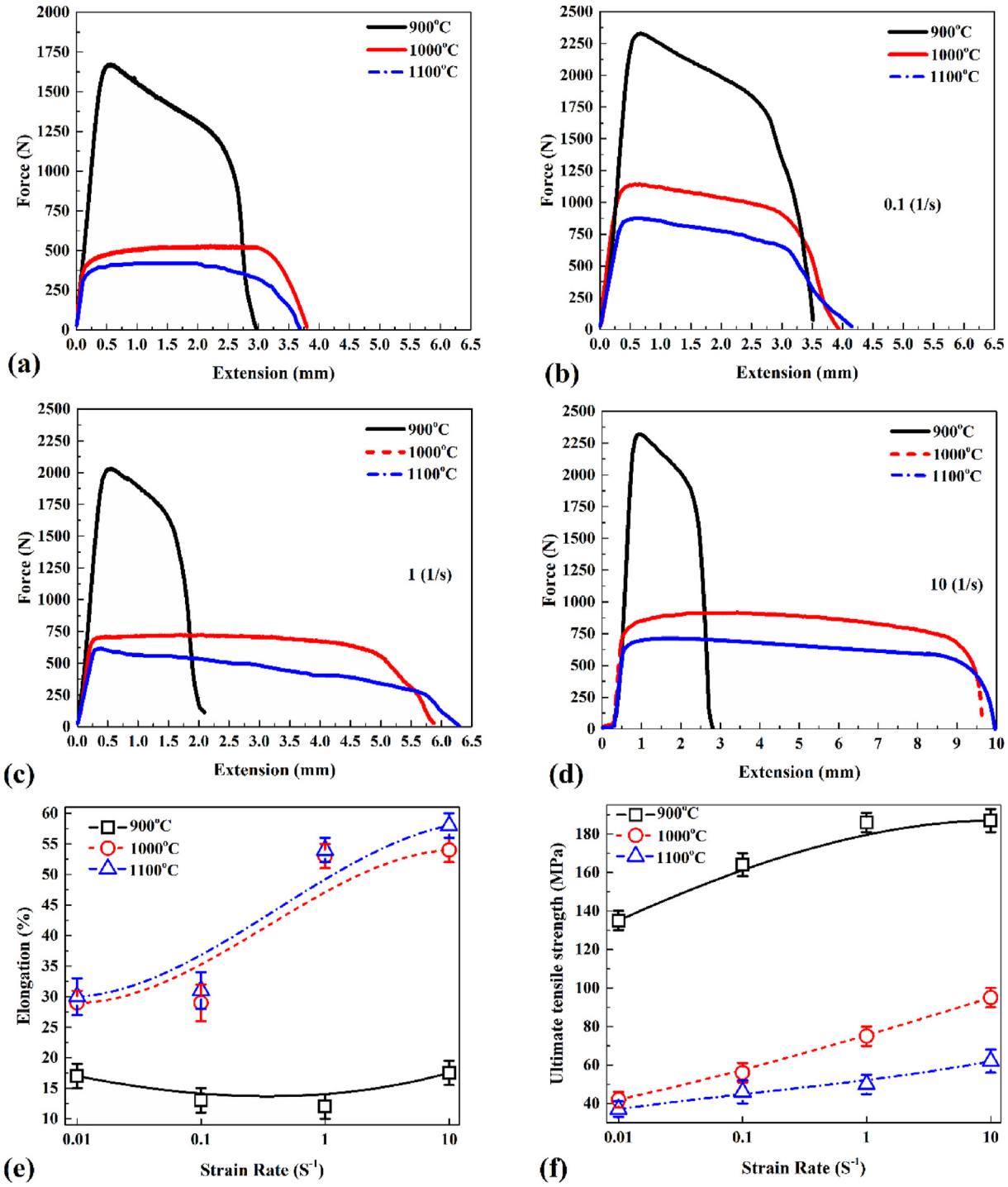


**Fig. 2 – Load-displacement curves of hot tensile samples at (a) 0.01s$^{-1}$, (b) 0.1s$^{-1}$, (c) 1s$^{-1}$ and (d) 10s$^{-1}$ strain rate. The relation with strain rate and (e) elongation and (f) ultimate tensile strength of tested samples.**

between samples 9 and 12 was used to analyse strain rate effects.

## 3. Results and discussion

The results from hot tensile tests and post-test analysis are presented and discussed in the following sections.

### 3.1. *Flow curves*

The load-displacement curves for tests with 0.01s$^{-1}$, 0.1s$^{-1}$, 1s$^{-1}$, and 10s$^{-1}$ strain rates are presented in Fig. 2a, b, 2c and 2d, respectively. The graphs can be divided into three stages, first, from starting to reaching the maximum point. In this stage, the flow stress of super Cr13 increases from zero to peak value due to work-hardening phenomena. After that, the

stable deformation phase appears in the graph, which indicates that dynamic recovery (DRV) and dynamic recrystallization (DRX) phenomena happen inside the super Cr13 sample during the test [20]. The final stage is related to the stretching phase, where the micro-voids arise inside the material and the flow curve starts to decrease. At the last stage, the load-bearing capacity of super Cr13 decreases gradually, and the final fracture occurs in the tensile sample [21]. The super Cr13 steel is a high Stacking-fault energy metal which means the dislocation mobility inside of this steel is increased when increasing temperature and applied load [22].

After reaching the highest point in the load-displacement curve, the work-hardening phenomenon gradually weakens, and softening of the super Cr13 starts. The experimental results show that the ultimate tensile strength (UTS) of super Cr13 stainless steel decreases with increasing temperature. The UTS of super Cr13 steel is dramatically dropped from 900 °C to 1000 °C in all strain rates. On the other hand, the elongation of samples increases, which means dynamic softening inside the super Cr13 is growing by increasing the test temperature.

This phenomenon means that the deformation resistance of super Cr13 is decreased with increasing temperature, fast dislocation mobility occurs, and DRV and DRX are initiated inside the super Cr13. This behaviour is detectable at all strain rates. The analysis of the effect of strain rate shows that the deformation of super Cr13 increases with increasing strain rate. Accordingly, it can be concluded that this steel has the potential for the hot deformation manufacturing process at a high strain rate. The results of elongation and ultimate tensile strength (UTS) of hot-tested samples are depicted in Fig. 2e and f, respectively. As mentioned in the curves, the highest elongation was recorded at 1100 °C with a $10s^{-1}$ strain rate. The elongation of the tensile sample increases with strain rate from $0.01s^{-1}$ to $10s^{-1}$ for all testing temperatures. The elongation of the sample that tested with 10 $s^{-1}$ at 900 °C was 2% more than that of 0.01 $s^{-1}$ at 900 °C. Similarly, the elongation of 1000 °C ($10s^{-1}$) and 1100 °C ($10s^{-1}$) was 21% and 24% higher than samples that tested at 1000 °C ($0.01s^{-1}$) and 1100 °C ($0.01s^{-1}$), respectively. The difference between the elongation of tensile samples in $0.01s^{-1}$ (~17%) was lower than the difference between the elongation of tensile samples in $10s^{-1}$ (~36%). The trend of UTS of samples is generally similar to tensile samples elongation. The UTS of the super Cr13 sample, from $0.01s^{-1}$ to $10s^{-1}$, increased 12 MPa, 24 MPa, and 31 MPa, respectively, at 900 °C, 1000 °C, and 1100 °C. The difference between the UTS of tensile samples in $0.01s^{-1}$ was ~100 MPa, and the difference between UTS of samples in $10s^{-1}$ was ~132 MPa. These results show that the super Cr13 behaviour at low strain rate is more ductile than at high strain rate.

### 3.2. *Microstructural analysis*

The microstructure of as-received super Cr13 is shown in Fig. 1a. The optical microscopy micrographs have been taken from different areas of the sample. The analysis shows a homogenous microstructure constituent distribution in the samples, and there is no significant difference between the side surfaces and centre of the super Cr13 before the hot tensile test. The results indicate that the as-delivered super Cr13 stainless steel has a tempered martensitic structure and a small amount of δ-ferrite.

As described earlier the samples 1 and 9 was considered to investigate the effects of temperature on the microstructure. Also, the microstructure of samples 9 and 12 were considered for effects of strain rate after hot tensile tests. The ternary iron-chromium-carbon constitution diagram for super Cr13 stainless steel is depicted in Fig. 3a. Due to the selected temperature domain during the tensile test (blue line in Fig. 3a), the microstructure in the test at 1100 °C was austenitic plus δ-ferrite. It means the microstructure of samples at 900 °C and 1000 °C before the test contains an austenite phase without carbides [23]. The image processing results from the average microstructure size (by histogram) of samples 1, 9, and 12 are presented in Fig. 3b, c and 3d, respectively. The results indicate that the average grain size of samples 1, 9, and 12 are 9.7 μm, 9.0 μm, and 7.8 μm, respectively. The average grain size of the tensile sample at 900 °C–1000 °C after the test decreased by ~8%. The increasing strain rate from $0.01s^{-1}$ to $10s^{-1}$ after the test led to a decreasing grain size by ~13%. As described in the experimental section, the hot tensile samples are quenched in room temperature water after this test. For this reason, the analysed microstructure incorporates the effects of post-heat treatment.

With 0.03% of carbon, the super Cr13 stainless steel is categorized as low-carbon martensitic steel. As mentioned earlier, the as-received material microstructure contains a martensite matrix with δ-ferrite. The presence of δ-ferrite in super Cr13 steel depends on chemical composition and thermo-mechanical actions [24]. Cr and Mo in the chemical composition of super Cr13 act as ferrite stabilizers, while C and Ni are austenite stabilizers. Generally, δ-ferrite is the undesirable phase in low-carbon martensitic steels, and the presence of δ-ferrite directly depends on the heat treatment of steel or thermo-mechanical action [25]. The δ-ferrite has compositional differences and lack of cohesion with the martensite matrix in super Cr13. For this reason, the δ-ferrite phase in the microstructure of super Cr13 steel deteriorates the hardness and mechanical properties. Also, compared to austenite, the ferrite phase is weak and, during high strain rate deformation, increases the risk of rupture [26]. Understanding microstructure changes are necessary to improve the analysis of the effects of temperature and strain rate. The microstructure of samples 1, 9, and 12 are depicted in Fig. 4a, b, and 4c, respectively. As mentioned above, the analysis of the hot deformation procedure has shown that the microstructure of super Cr13 changes to the austenite phase before the test. The comparison of samples 1 and 9 shows a higher amount of retained austenite and δ-ferrite in the martensite matrix in sample 9. This comparison refers to the effects of test temperature, which shows that increasing testing temperature increases the amount of δ-ferrite in super Cr13. The retained austenite denotes the amount of austenite that, during the cooling stage of the tensile test has not been fully converted into martensite. After the tensile test, the super Cr13 sample exhibits stress-induced deformation. With increasing strain rate, the stress-induced deformation is increased as well. The stress-induced deformation leads to martensite transformation. Comparing sample 9 and sample 12 a new martensite phase in the microstructure of sample 12

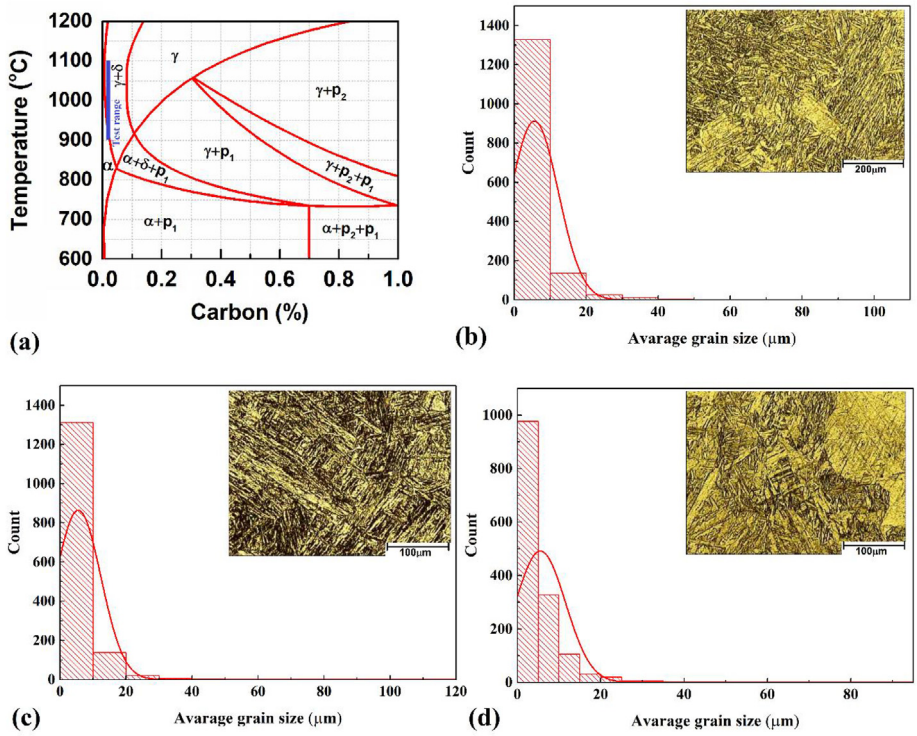


**Fig. 3 – (a) Ternary iron-chromium-carbon constitution diagram for super Cr 13 stainless steel. Histogram of average grain size from (b) sample 1, (c) sample 9 and (d) sample 12.**

can be seen, which is the result of the higher strain rate (as higher stress-induced deformation). With the higher magnification of microstructures, new phases have been detected locally. In addition to mentioned phases, Austenitic-martensite (AM) was detected in the microstructure. The AM is a mixture structure consisting of fine lath martensite (FLM) and filmy retained austenite with a thin shape. In some local areas, a mixture of filmy retained austenite (FRA) with coarse lath martensite (CLM) was detected. This mixture is formed inside an austenite structure, and a couple of carbides ($C_b$) are trapped inside the martensite lath. For a better understanding of the described structure, a schematic view is presented in

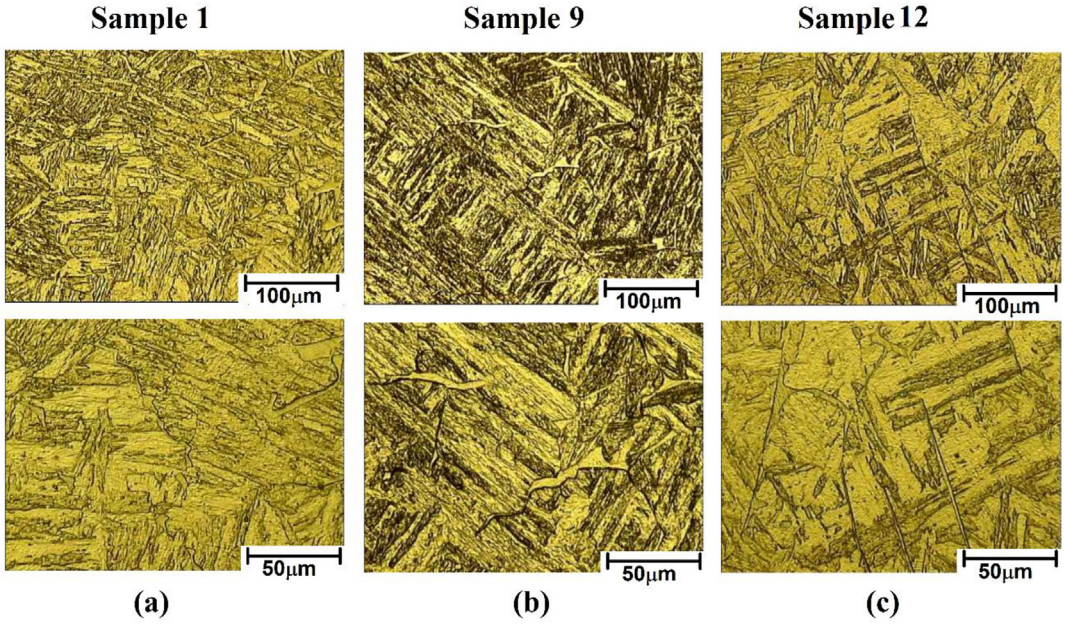


**Fig. 4 – Microstructure of sample (a) 1, (b) 9 and (c) 12.**

Fig. 5a. The high-magnification optical microscopy images from samples 1, 9, and 12 are presented in Fig. 5b, c and 5d, respectively. The results show that with increasing temperature of the test, the amount of carbides decreases, and on the other hand, the presence of δ-ferrite increased in high strain rate samples. Comparing samples 9 and 12 shows that elongated δ-ferrite is formed at the strain rate of $10s^{-1}$, and this type of δ-ferrite does not exist in low strain rate samples.

### 3.3. *XRD analysis*

The XRD results of super Cr13 stainless steel are depicted in Fig. 6a. The obtained results show that the as-delivered material has retained austenite and martensite. The diffraction peaks (311), (220), and (200) indicate the retained austenite phase with a face-centered cubic (FCC) structure. The martensite phase is detectable by diffraction lines (211), (200), and (110) that represent the body-centered cubic (BCC) unit cell structure. The XRD analysis results performed on Samples 1, 9, and 12 are presented in Fig. 6b, c and 6d, respectively.

The XRD results of sample 1 indicated the retained austenite (FCC phase) and martensite/austenite peaks and martensite. With increasing test temperature, the austenite phase decreased, and peaks of $M_{23}C_6$ carbides ($Cr_{23}C_6$) and $Cr_2N$ carbide appeared generally. In the obtained results, carbides are detectable by diffraction lines (400), (531), and (600). The peaks of carbides are intense in sample 1. With increasing the test temperature from 900 °C to 1100 °C, the peak intensity of carbides is reduced. This effect seems related to the dissolution of carbides into steel. As shown in the microstructural analysis, the carbides can be more easily detected in sample 1 than in the other cases. On the other hand, with increasing strain rate, the intensity for all peaks is moderated, which means the presence δ-ferrite and austenite in the martensite matrix increased, and the structure had a small number of carbides. The chemical analysis of XRD

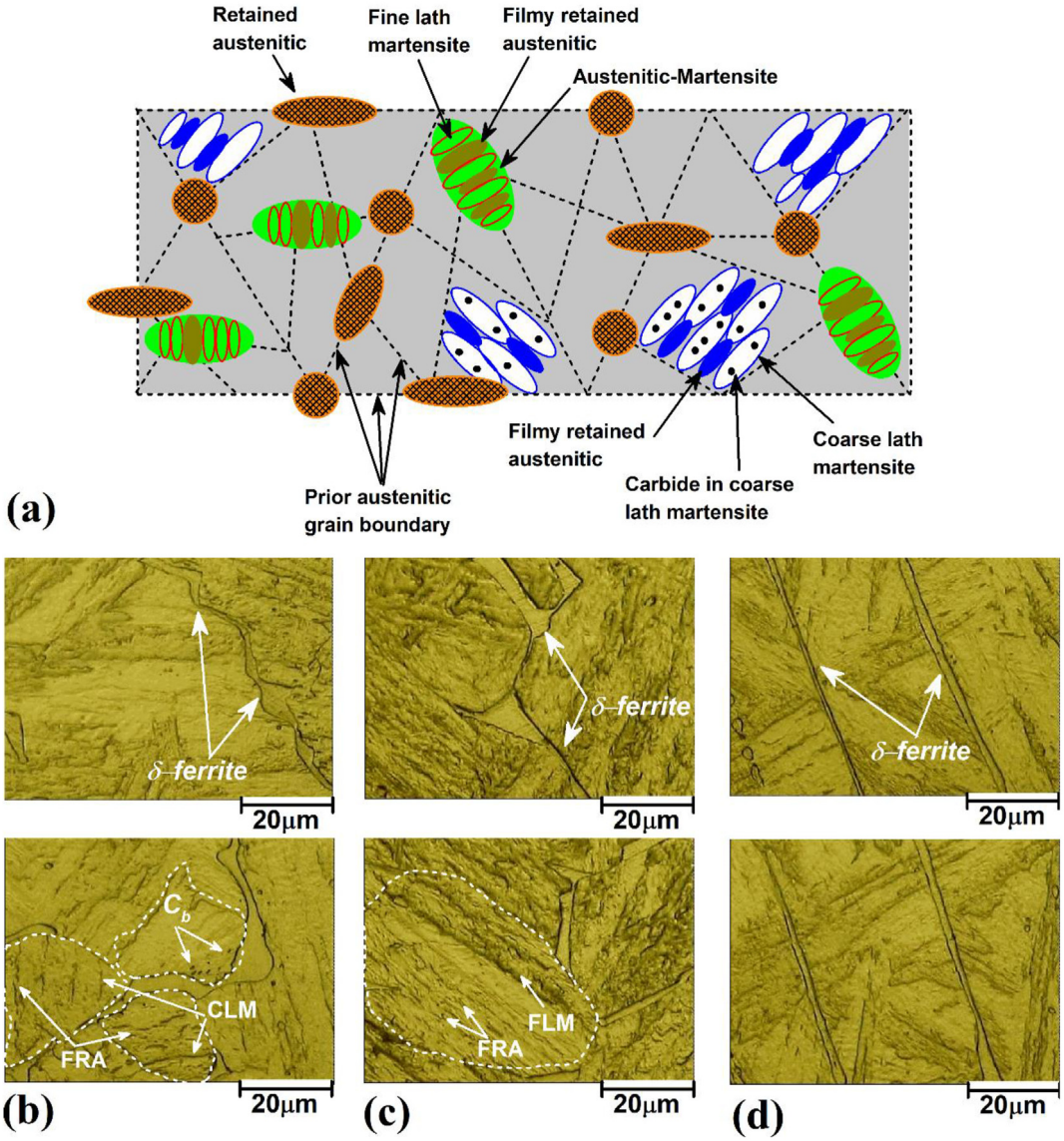


**Fig. 5 – (a) schematics of various phases in tensile sample after the test. High magnification of optical microscopy image from microstructure of (b) sample 1, (c) sample 9 and (d) sample 12.**

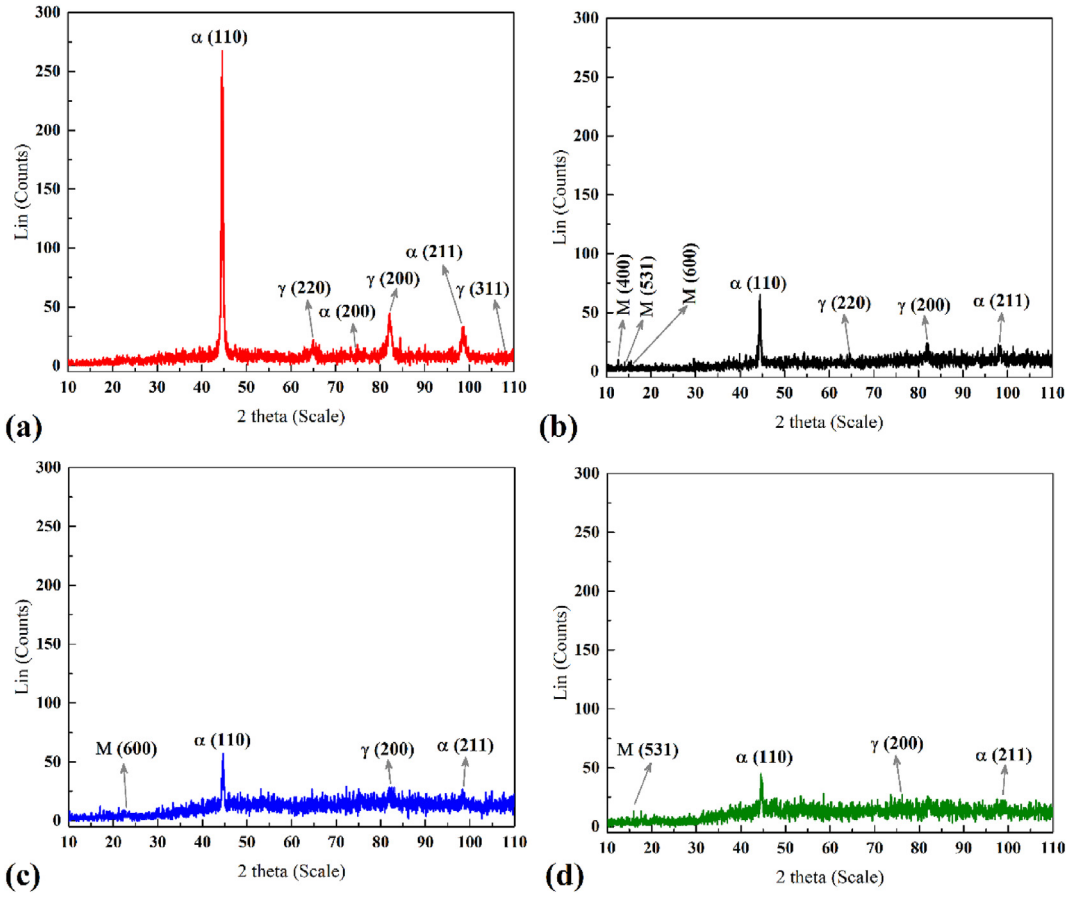


**Fig. 6 – XRD results of (a) raw super Cr13, (b) sample 1, (c) sample 9 and (d) sample 12.**

results revealed that the main structures in as-delivered super Cr13 were Fe, Fe–Ni, Fe–Cr, and Ni–Cr–Fe. The results show that after the hot deformation test, Fe–C and Fe–Cr–C precipitates were formed in samples 1, 9, and 12, and any evidence of Fe–Ni–C precipitation was not detected.

### 3.4. *Hardness changes*

The Vickers Hardness (HV) of as-delivered super Cr13 was measured in the centre of the sample. Results show that the hardness level along the radius of the tensile sample was almost uniform. The average hardness of the as-received sample was 387 $HV_{0.3}$. The hardness of samples 1, 9, and 12 were measured to investigate the temperature and strain rate effects on the hardness. The centre of the hardness sample is set as 0 and measured every 0.5 mm across the radius of the sample. The left side is signed by minus, and the right side is signed by plus. The hardness results as a function of distance from the centre of the sample are depicted in Fig. 7. The general trend shows that the hardness of hot tensile samples is lower than as-received super Cr13 steel. Also, the overall survey shows that the hardness in the centre is slightly higher than in the sides. The average hardness of sample 1 was 382 $HV_{0.3}$. Increasing the temperature from ambient to 900 °C increased the amount of martensite, and the appearance of precipitates led to the hardness of this sample to be closer to the as-delivered super Cr13. With increasing the test temperature, the hardness decreases. The average hardness of sample 9 is 370 $HV_{0.3}$. The main reason is the dissolution of precipitates and the increasing amount of δ-ferrite. On the other hand, comparing the hardness of samples 9 and 12 shows that increasing the strain rate during the hot tensile

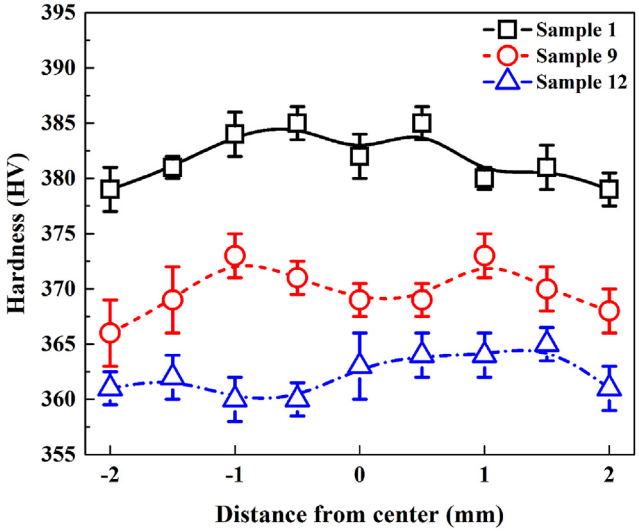


**Fig. 7 – Hardness results of samples 1, sample 9 and sample 12.**

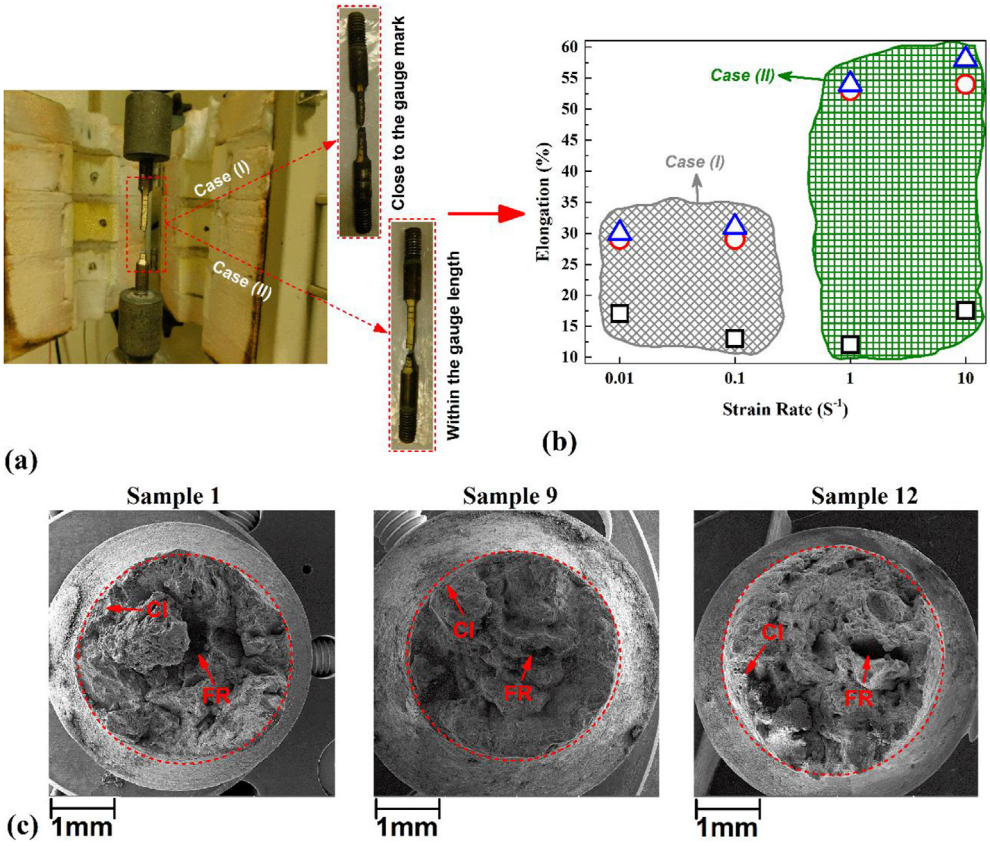


**Fig. 8 – (a) Image of case (I) and case (II) fracture type, (b) relation between strain rate and fracture type. (c) Low magnification SEM image from fracture surface of samples 1, 9 and 12.**

test of super Cr13 results in reduced hardness. As discussed before, the bigger and elongated δ-ferrite formed in sample 12 leads to a smaller amount of martensite, causing a decrease in hardness to 366 $HV_{0.3}$ in sample 12.

### 3.5. *Fractography analysis*

The fracture behaviour of hot tensile test samples is analysed in this section. The obtained results show two types of ruptures in the hot tensile samples. The tensile sample was broken within the gauge length in the first type, case (I). In the second type, case (II), the tensile sample was broken close to the gauge mark after the test. A picture of the fracture type of case (I) and (II) is presented in Fig. 8a. All tensile samples after the test were broken with these two fracture modes. The results show that hot tensile samples tested at $0.01s^{-1}$ and $0.1s^{-1}$ strain rates were broken in case (I) mode, and others were broken in case (II) mode (Fig. 8b). The low magnification SEM image from samples 1, 9 and 12 are presented in Fig. 8c. During the hot tensile test, the crack initiate (CI) from the exterior side of super Cr13 and grows inwards until final rupture (FR) occurs from the middle of the tensile sample. This trend is observed for all samples independent of the test temperature and strain rate.

SEM micrographs of fracture morphologies from sample 1 is depicted in Fig. 9. The fracture surface shows a complex morphology that consists of small dimples. The fracture surface at high magnification revealed cleavages and intergranular cracks as well. These features indicates a ductile fracture, but all morphologies are local and can be detected in high magnification. Some stretching areas can be detected in low-magnification SEM images, and the fracture surface was not fully ductile. Cleavage morphology usually occurs over dense atomic planes and can be detected in over-dense atomic planes [27].

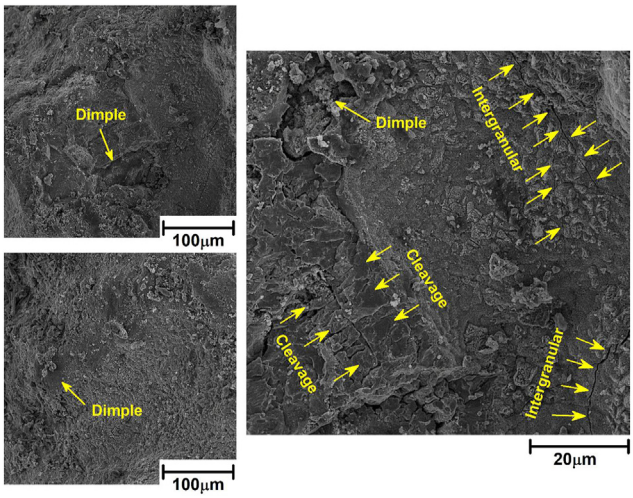


**Fig. 9 – SEM image from fracture surface of sample 1.**

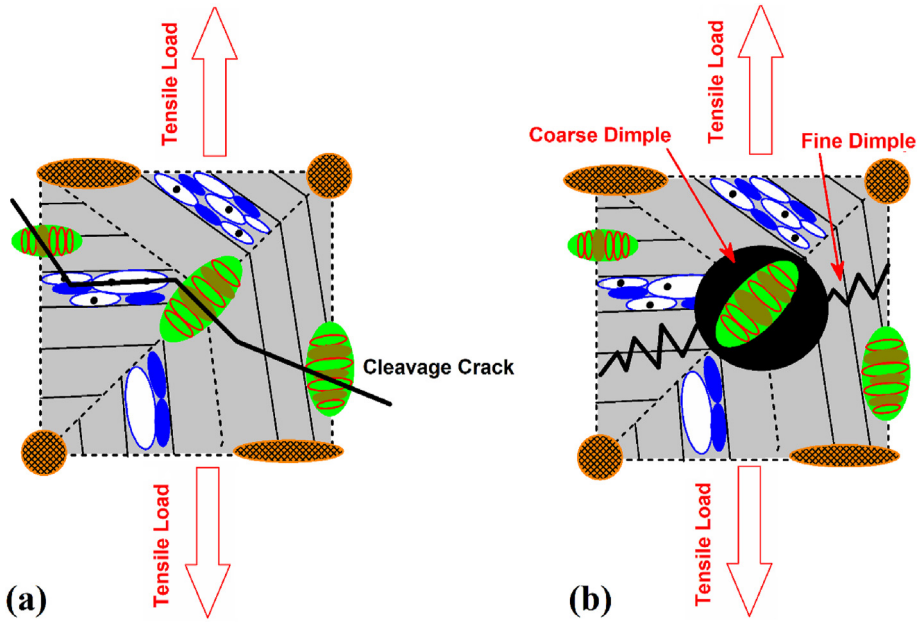


**Fig. 10 – Schematic view of (a) brittle and (b) ductile fracture mechanism during hot tensile test of Super Cr13.**

Presence of BCC structure in the steel increase the formation of cleavage in the fracture surface. As mentioned before in the XRD section, intense peaks of (211), (200), and (110) show BCC structures in sample 1. Other phenomena detected on the sample 1 fracture surface were elongated cracks. These elongated cracks are related to the intergranular fracture, which shows brittle failure mode. This crack type is caused by the segregation of impurities at grain boundaries [28]. It seems the $C_b$ made this morphology on the fracture surface of sample 1. For a better understanding of the fracture behaviour in this sample, an illustration is presented in Fig. 10a. During applied tensile stress on sample 1, the initiated cleavage cracks from the side of sample grows along the inside of the grain structures. For this reason, small dimples (as a crack-initiated zone) and intergranular cracks were detected. It is stated that retained austenite produced by strain-induced transformation suppresses cleavage crack initiation [29]. On the other hand, the presence of the austenite-martensite phase retards the cleavage crack growth [30]. The mixture of various phases in super Cr13 made a complex fracture surface.

In Fig. 10b, a schematic view of ductile fracture is depicted. Various information like void initiation, crack growth, and void coalescence can be found in ductile fracture surfaces. The difference between brittle and ductile fracture of super Cr 13 during the hot tensile test is crack initiation (void initiation). The cracks initiate at the interface of the austenite-martensite phase and martensitic matrix. On the other hand, due to the weak bonding of δ-ferrite and martensite, this area is the main potential point for crack initiations. Like brittle fracture, the crack initiation was supressed by retained austenite with strain-induced martensite transformation. With further progress of the hot tensile test, the generated voids start to grow and unify. A short austenite-martensite phase decreases the possibility of crack initiation, while the

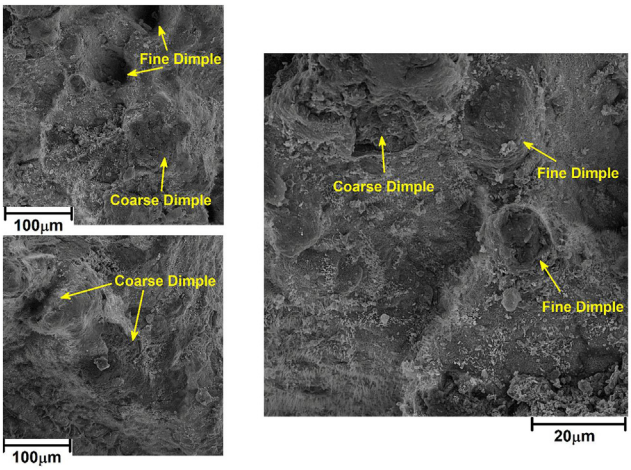


**Fig. 11 – SEM image from fracture surface of sample 9.**

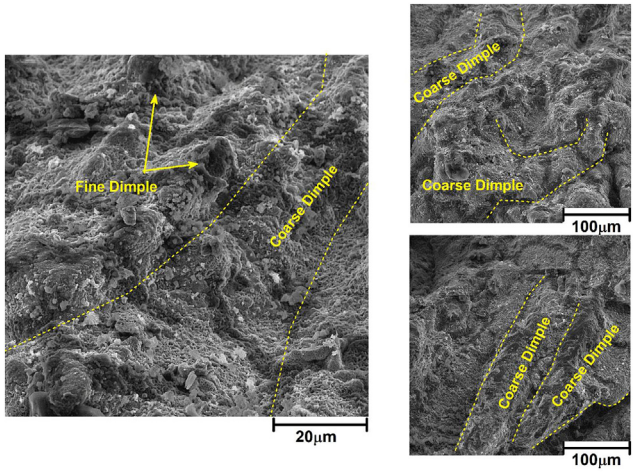


**Fig. 12 – SEM image from fracture surface of sample 12.**

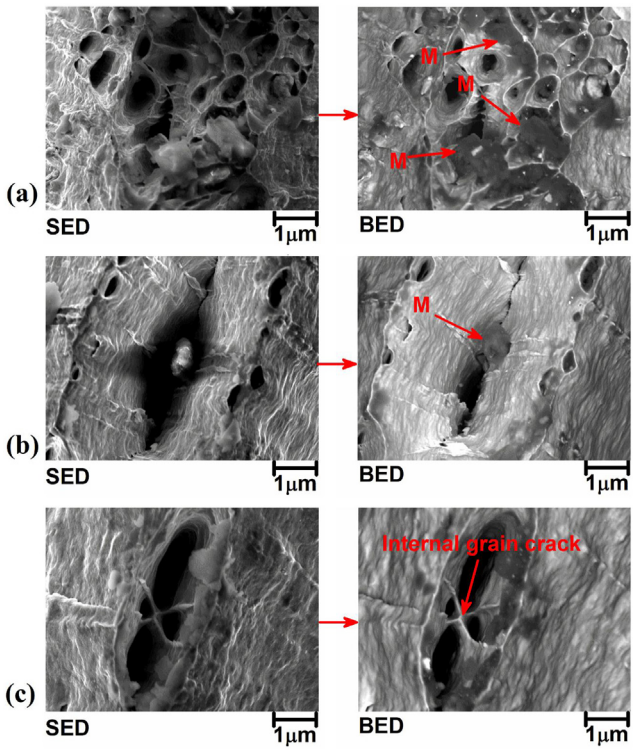


**Fig. 13 – SED and BED SEM image from fracture surface of samples (a) 1, (b) 9, and (c) 12.**

presence of large austenite-martensite phase increases the possibility of crack initiation.

The SEM image of sample 9 and sample 12 are presented in Figs. 11 and 12, respectively. The difference between sample 1 and sample 9 is the testing temperature, since both were tested at in $0.01s^{-1}$ strain rate. In this case, it can be concluded that the test temperature made the main difference in the morphology of the fracture surface. As the results show, the fracture surface of sample 9 consists of fine and coarse dimples. The number of fine dimples is high, as seen in the high magnification SEM image. This indicates that the number of austenite-martensite phases was higher in sample 9 (mentioned in the microstructure section) compared to sample 1. However, a higher number of fine dimples indicates that the austenite-martensite phases were short and close together. For this reason, a high number of fine dimples were formed during crack unifying (as depicted in Fig. 10b). On the other hand, the fracture surface of sample 12 showed harsher and elongated coarse dimples. Comparing the fracture surface morphology of sample 12 with sample 9 revealed that at a high strain rate, crack initiation was supressed by strain-induced martensite transformation in super Cr13. The high strain rate increase supresses crack initiation by increasing martensite transformation. This phenomenon prevents the formation of fine dimples, stretching super Cr13 during the hot tensile test, and rapid fracture by coarse dimple formation.

The magnification SEM image from fracture surfaces for analysis of precipitates is presented in Fig. 13. The SEM images show the precipitate (M) points in samples 1, 9, and 12.

Due to ultra-high magnification, these phenomena are local. The secondary electron detector (SED) image and the Backscattered electrons detector (BED) have been used for better analysis. The SED image used for local fracture analysis (similar to Figs. 10–12). Moreover, BED images are used to analyse alloy detection by colour contrast. As discussed before, a couple of dimples were detected in Sample 1. In Fig. 13a, small dimples can be seen as well. These dimples are tiny. On the other hand, the BED image revealed the dark materials stuck inside the dimple holes. These are the

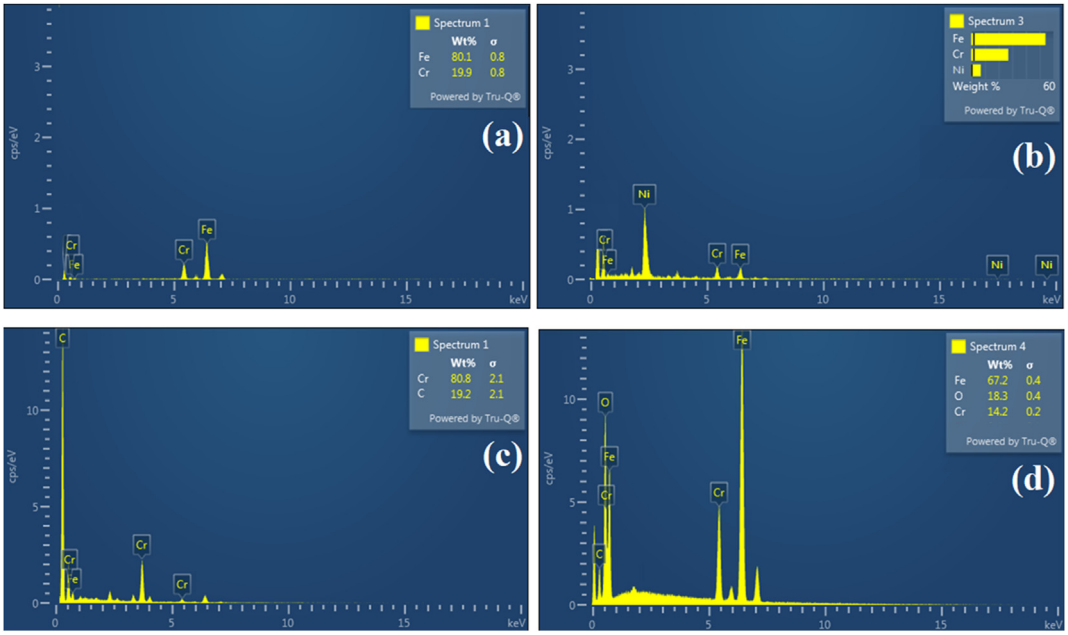


**Fig. 14 – (a) and (b) EDS point analysis from precipitates of sample 1. (c) and (d) EDS point analysis from precipitates of sample 9.**

carbides trapped inside coarse martensite lath and exposed after the tensile test at sample 1. The SEM image indicated the fracture surface of the austenite-martensite structure. The BED image exposed the trapped precipitated inside of martensite in of austenite-martensite structure. The SED and BED images from the fracture surface of sample 9 are presented in Fig. 13b the picture shows a bigger dimple than sample 9 because the image of Fig. 13a is shown a fine dimple, and the image of 13b shows a coarse dimple. Similar to sample 1, a small precipitate was trapped inside the dimple in sample 9 that pointed in the BED image. The SED and BED images from the fracture surface of sample 12 are presented in Fig. 13c. The results show a cross-link inside the dimple. This effect happened when the crack growth inside the grain boundaries detailed in Fig. 10b.

A sample of EDS point analysis from M points inside the fracture surface dimples of sample 1 is shown in Fig. 14a and b. For analysis of precipitates in the fracture surface of sample 9, the point EDS analysis was carried out, and the results are presented in Fig. 14c and d. The results show that the precipitates are Fe–Ni, Fe–Cr, and Ni–Cr–Fe with high chromium carbides. The EDS point results indicated the carbon-rich precipitate that proves the M23C6 precipitates already shown in XRD results. A mixture of precipitates is detected that shows a complex chemical reaction during the cooling stage. The Ni–Cr–Fe complex is seen in samples 1 and 9, and more M23C6 precipitates were detected in sample 1.

## 4. Conclusions

The hot tensile behaviour of super Cr13 stainless steel has been studied. The test temperature range was from 900 °C to 1100 °C, and the strain rates were from $0.01s^{-1}$ to $10s^{-1}$. The main conclusions from this work are as follows.

1. The results show that the ultimate tensile strength of super Cr13 steel decreases with increasing the test temperature from 900 °C to 1100 °C. On the other hand, with an increasing test strain rate from $0.01s^{-1}$ to $10s^{-1}$, the elongation of the tensile sample increases. The lowest UTS obtained in 1100 °C ($0.01s^{-1}$) sample (~34 MPa), and the highest UTS obtained in 900 °C ($10s^{-1}$) Sample (~187 MPa).
2. The microstructural analysis revealed that an elongated δ-ferrite phase is formed in the microstructure of the samples that were tested at a high strain rate. $Cr_{23}C_6$ and $Cr_2N$ carbides were detected in the microstructure of samples tested below 1000 °C. The carbides dissolved when the testing temperature was higher than 1000 °C. The amount of retained austenite increased by increasing the test temperature.
3. The XRD results revealed that Fe–Ni, Fe–Cr, and Ni–Cr–Fe formed the main precipitates in the super Cr13 steel after the hot tensile test. Increasing retained austenite and δ-ferrite at high strain rate and temperature decreases the amount of martensite phase and the hardness of tensile samples.
4. The tensile sample surface after the test revealed brittle-ductile fracture morphology in samples tested at low temperature and strain rate. This fracture morphology consists of dimples, cleavages, and intergranular cracks. The results show big coarse dimples with a partial fine dimple on the fracture surface of the sample tested at high temperatures and high strain rates. This fracture morphology indicates fast crack growth during the test.

## Declaration of competing interest

The authors declare that they have no known competing financial interests or personal relationships that could have appeared to influence the work reported in this paper.

## Acknowledgement

This project has received funding from the European Union's Horizon 2020 Research and Innovation Programme under the Marie Skłodowska-Curie grant agreement No. 847624. In addition, a number of institutions back and co-finance this project. The paper reflects only the authors' view and the Agency is not responsible for any use that may be made of the information it contains.

## REFERENCES

[1] Badkoobeh F, Mostaan H, Rafiei M, Bakhsheshi-Rad HR, Berto F. Microstructural characteristics and strengthening mechanisms of ferritic–martensitic dual-phase steels: a review. Metals 2022;12:101. https://doi.org/10.3390/met12010101.
[2] Derazkola HA, Gil EG, Murillo-Marrodán A, Méresse D. Review on dynamic recrystallization of martensitic stainless steels during hot deformation: Part i—experimental study. Metals 2021:11.
[3] Chen H, Zhao L, Lu S, Lin Z, Wen T, Chen Z. Progress and perspective of ultra-high-strength martensitic steels for automobile. Metals 2022;12:2184. https://doi.org/10.3390/met12122184.
[4] El-Aziz KA, Saber D. Mechanical and microstructure characteristics of heat-treated of high-Cr WI and AISI4140 steel bimetal beams. J Mater Res Technol 2020;9:7926–36. https://doi.org/10.1016/j.jmrt.2020.05.017.
[5] Lenda O Ben, Tara A, Lazar F, Jbara O, Hadjadj A, Saad E. Structural and mechanical characteristics of AISI 420 stainless steel after annealing. Strength Mater 2020;52:71–80. https://doi.org/10.1007/s11223-020-00151-4.
[6] Giordana MF, Alvarez-Armas I, Armas A. On the cyclic softening mechanisms of reduced activity ferritic/martensitic steels. Steel Res Int 2012;83:594–9. https://doi.org/10.1002/srin.201100254.
[7] He J, Han G, Feng Y. Phase transformation and plastic behavior of QP steel sheets: transformation kinetics-informed modeling and forming limit prediction. Thin-Walled Struct 2022;173:108977. https://doi.org/10.1016/j.tws.2022.108977.
[8] Huang Y, Yang J, Feng R, Chen H. Resistance of cold-formed sorbite stainless steel circular tubes under uniaxial compression. Thin-Walled Struct 2022;179:109739. https://doi.org/10.1016/j.tws.2022.109739.
[9] Wróbel I, Skowronek A, Grajcar A. A review on hot stamping of advanced high-strength steels: technological-metallurgical aspects and numerical simulation. Symmetry (Basel). 2022;14:969. https://doi.org/10.3390/sym14050969.

[10] Aghajani Derazkola H, Garcia E, Murillo-Marrodán A. Effects of tool–workpiece interfaces friction coefficient on power and energy consumption during the piercing phase of seamless tube production. J Mater Res Technol 2022;19:3172–88. https://doi.org/10.1016/j.jmrt.2022.06.071.
[11] Topa A, Cerik BC, Kim DK. A useful manufacturing guide for rotary piercing seamless pipe by ALE method. J Mar Sci Eng 2020;8:756. https://doi.org/10.3390/jmse8100756.
[12] Aghajani Derazkola H, Garcia E, Murillo-Marrodán A, Conde Fernandez A. Review on modeling and simulation of dynamic recrystallization of martensitic stainless steels during bulk hot deformation. J Mater Res Technol 2022;18:2993–3025. https://doi.org/10.1016/j.jmrt.2022.03.179.
[13] Momeni A, Dehghani K. Prediction of dynamic recrystallization kinetics and grain size for 410 martensitic stainless steel during hot deformation. Met Mater Int 2010;16:843–9. https://doi.org/10.1007/s12540-010-1024-5.
[14] Li J, Zhan D, Jiang Z, Zhang H, Yang Y, Zhang Y. Progress on improving strength-toughness of ultra-high strength martensitic steels for aerospace applications: a review. J Mater Res Technol 2023;23:172–90. https://doi.org/10.1016/j.jmrt.2022.12.177.
[15] Liu W, Li J, Li S, Li J, Li X. Effect of nitrogen on the hot deformation behavior of 0.4C–13Cr martensitic stainless steel. Steel Res Int 2021;92:2100020. https://doi.org/10.1002/srin.202100020.
[16] Shaikh A, Churyumov A, Pozdniakov A, Churyumova T, Li H, Fan G, He Y, Bai J, Zhang C, Han P. Simulation of the hot deformation and fracture behavior of reduced activation ferritic/martensitic 13CrMoNbV Steel. Steel Res Int 2015;86:84–8. https://doi.org/10.3390/app10020530.
[17] Deng Y, Li J, Li W, Gu J, Zhang X. Strain rate dependence of hot tensile behavior, microstructure evolution, and fracture mechanism of lean duplex stainless steel 2101. Steel Res Int 2022;93:2100444. https://doi.org/10.1002/srin.202100444.
[18] Salas-Reyes AE, Altamirano-Guerrero G, Chávez-Alcalá JF, Barba-Pingarrón A, Figueroa IA, Bolarín-Miró AM, Sánchez-De Jesús F, Deaquino-Lara R, Salinas A. Influence of boron content on the solidification structure, magnetic properties and hot mechanical behavior in an advanced as-cast TWIP steel. Metals 2020;10.
[19] No Title Available online: https://www.tubosreunidosgroup.com/en/home.
[20] Sakai T, Belyakov A, Kaibyshev R, Miura H, Jonas JJ. Dynamic and post-dynamic recrystallization under hot, cold and severe plastic deformation conditions. Prog Mater Sci 2014;60:130–207. https://doi.org/10.1016/j.pmatsci.2013.09.002.
[21] Zou D, Han Y, Yan D, Wang D, Zhang W, Fan G. Hot workability of 00Cr13Ni5Mo2 supermartensitic stainless steel. Mater Des 2011;32:4443–8. https://doi.org/10.1016/j.matdes.2011.03.067.
[22] Wang P, Xiao N, Lu S, Li D, Li Y. Investigation of the mechanical stability of reversed austenite in 13%Cr-4%Ni martensitic stainless steel during the uniaxial tensile test. Mater Sci Eng, A 2013;586:292–300. https://doi.org/10.1016/j.msea.2013.08.028.
[23] Godin H, Mithieux J-D, Parrens C, Badinier G, Sennour M, Gourgues-Lorenzon A-F. Effects of cooling path and resulting microstructure on the impact toughness of a hot stamping martensitic stainless steel. Mater Sci Eng, A 2019;742:597–607. https://doi.org/10.1016/j.msea.2018.11.036.
[24] Kang SE, Kang MH, Mintz B. Influence of vanadium, boron and titanium on hot ductility of high Al, TWIP steels. Mater Sci Technol 2021;37:42–58. https://doi.org/10.1080/02670836.2020.1861736.
[25] Niessen F. Austenite reversion in low-carbon martensitic stainless steels – a CALPHAD-assisted review. Mater Sci Technol 2018;34:1401–14. https://doi.org/10.1080/02670836.2018.1449179.
[26] Steenken B, Rezende JLL, Senk D. Hot ductility behaviour of high manganese steels with varying aluminium contents. Mater Sci Technol 2017;33:567–73. https://doi.org/10.1080/02670836.2016.1235855.
[27] Pineau A, Benzerga AA, Pardoen T. Failure of metals I: brittle and ductile fracture. Acta Mater 2016;107:424–83. https://doi.org/10.1016/j.actamat.2015.12.034.
[28] Sugimoto KI. Recent progress of low and medium-carbon advanced martensitic steels. Metals 2021:11.
[29] Sugimoto K, Tanino H, Kobayashi J. Impact toughness of medium-Mn transformation-induced plasticity-aided steels. Steel Res Int 2015;86:1151–60. https://doi.org/10.1002/srin.201400585.
[30] Kobayashi J, Ina D, Nakajima Y, Sugimoto K. Effects of microalloying on the impact toughness of ultrahigh-strength TRIP-aided martensitic steels. Metall Mater Trans A 2013;44:5006–17. https://doi.org/10.1007/s11661-013-1882-9.